The Astrophysical Journal Letters, 909:L29 (8pp), 2021 March 10 https://doi.org/10.3847/2041-8213/abeb6f

A CO Survey of SpARCS Star-forming Brightest Cluster Galaxies: Evidence for Uniformity in BCG Molecular Gas Processing across Cosmic Time

Delaney A. Dunne[1], Tracy M. A. Webb[1], Allison Noble[2], Christopher Lidman[3,4], Heath Shipley[1], Adam Muzzin[5], Gillian Wilson[6], and H. K. C. Yee[7]

[1] McGill Space Institute, Department of Physics, McGill University, 3600 rue University, Montreal, QC H3A 2T8, Canada
[2] ASU School of Earth and Space Exploration, P.O. Box 871404, Tempe, AZ 85287, USA
[3] Research School of Astronomy and Astrophysics, Australian National University, Canberra ACT 2611, Australia
[4] Centre for Gravitational Astrophysics, College of Science, The Australian National University, ACT 2601, Australia
[5] Department of Physics and Astronomy, York University, 4700 Keele Street, Toronto, ON MJ3 1P3, Canada
[6] Department of Physics and Astronomy, University of California-Riverside, 900 University Avenue, Riverside, CA 92521, USA
[7] The David A. Dunlap Department of Astronomy and Astrophysics, University of Toronto, 50 St George Street, Toronto, ON M5S 3H4, Canada
Received 2021 February 11; revised 2021 March 1; accepted 2021 March 3; published 2021 March 17

Abstract

We present ALMA CO (2-1) detections of 24 star-forming brightest cluster galaxies (BCGs) over $0.2 < z < 1.2$, constituting the largest and most distant sample of molecular gas measurements in BCGs to date. The BCGs are selected from the Spitzer Adaptation of the Red-Sequence Cluster Survey (SpARCS) to be IR-bright and therefore star-forming. We find that molecular gas is common in star-forming BCGs, detecting CO at a detection rate of 80% in our target sample of 30 objects. We additionally provide measurements of the star formation rate and stellar mass, calculated from existing MIPS 24 μm and IRAC 3.6 μm fluxes, respectively. We find these galaxies have molecular gas masses of $0.7–11.0 \times 10^{10}\,M_{\odot}$, comparable to other BCGs in this redshift range, and specific star formation rates that trace the main sequence of Elbaz et al. We compare our BCGs to those of the lower-redshift, cooling-flow BCG sample assembled by Edge and find that at $z \lesssim 0.6$ the two samples show very similar correlations between their gas masses and specific SFRs. We suggest that, in this redshift regime, the $\sim$10% of BCGs that are star-forming process accreted molecular gas into stars through means that are agnostic to both their redshift and their cluster mass.

Unified Astronomy Thesaurus concepts: Galaxy clusters (584); Galactic and extragalactic astronomy (563); Brightest cluster galaxies (181); Galaxy evolution (594); Molecular gas (1073)

1. Introduction

Galaxy clusters are extreme examples of hierarchical structure formation, forming the largest overdensities in the primordial universe. Brightest cluster galaxies (BCGs), as massive galaxies residing in the dense, violent centers of galaxy clusters, evolve through pathways that are a direct result of this environment.

In the latter stage of their evolution (after $z \sim 1$), the stellar mass of BCGs roughly doubles (Lidman et al. 2012). While this is expected to be mostly a dry process done primarily through gasless mergers of the BCGs with infalling cluster galaxies (De Lucia & Blaizot 2007), some ($\sim$10%, based on a 24 μm flux $\geqslant$100 μJy; Webb et al. 2015) BCGs do show star formation at these redshifts. The mechanism driving this star formation is not clear. Possible scenarios include mergers, either major or minor, of the BCG with gas-rich infalling cluster galaxies, or large-scale "cooling flows" of gas from the intracluster medium (ICM) onto the BCG.

Galaxy clusters themselves are not a homogeneous population, complicating the search for a star formation mechanism in their centers. Early X-ray observations revealed that some cluster cores contain an ICM dense enough to cool hydrostatically on timescales much shorter than the Hubble time (e.g., Fabian & Nulsen 1977). As the ICM cools and compresses, hot gas from outer regions of the cluster flows in to replace it, causing a cooling flow. Located at the center of the cluster, the BCG is often the recipient of gas from the cooling flow. Indeed, some star-forming BCGs seem to have star formation attributable to cooling flows. Examples include the Phoenix cluster at $z = 0.596$ (McDonald et al. 2012; Russell et al. 2017) and SpARCS104922.6+564032.5 (SpARCS1049; Webb et al. 2017; Hlavacek-Larrondo et al. 2020) at $z = 1.709$.

A key tool in deciphering star formation processes is cool molecular hydrogen (H_2) gas, which acts as the fuel for future star formation in galaxies, and is commonly traced by the rotational transitions of CO (Solomon & Vanden Bout 2005). However, few studies have systematically measured the molecular gas content in BCGs over a range of redshifts. We aim to constrain the processes driving BCG mass growth by studying molecular gas in a large sample of BCGs spanning 6 Gyr of cosmic time.

In this paper, we present new ALMA measurements of the CO (2-1) transition in 30 BCGs, selected from the SpARCS survey (described in Section 2.1). Our sample is large, containing 24 CO detections, and extends to much higher redshifts ($z \sim 1.2$) than any previous statistical BCG survey. We introduce the SpARCS cluster sample, our ALMA observations, and our data reduction method in Section 2. In Section 3, we contextualize our BCGs' molecular gas with other field and cluster measurements. Section 4 discusses the implications of these observations for BCG mass growth, and we present our conclusions in Section 5. We use standard cosmology ($H_0 = 70\,\mathrm{km\,s^{-1}\,Mpc^{-1}}$; $\Omega_{\mathrm{matter}} = 0.3$; $\Omega_{\Lambda} = 0.7$) throughout.

2. Observations and Data Reduction

2.1. The Parent SpARCS Sample

The BCGs studied here are drawn from clusters in the Spitzer Adaptation of the Red Sequence Cluster Survey (SpARCS;

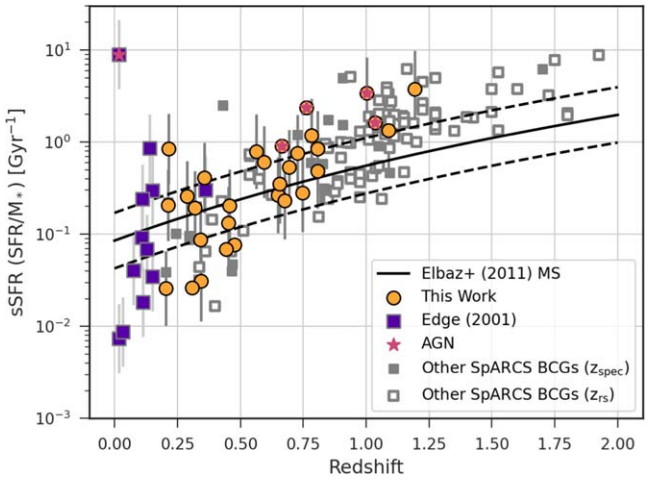

Figure 1. The specific star formation rates (sSFRs) of the BCGs in our sample (orange circles), the Edge (2001) sample (purple squares), and the parent SpARCS BCG sample we draw from (gray squares; Webb et al. 2015). Redshift values for this parent sample are principally the SpARCS RS-estimated redshifts ($z_{\rm RS}$; empty squares). Where available, we use spectroscopic redshifts ($z_{\rm spec}$; filled squares) from OzDES (Lidman et al. 2020) or the literature (Gunn et al. 1998; Swinbank et al. 2007; Adelman-McCarthy et al. 2008; Abazajian et al. 2009; Hernán-Caballero et al. 2009; Weedman & Houck 2009; Menzel et al. 2016). The Elbaz et al. (2011) sSFR MS is shown for comparison, with the scatter indicated with dashed lines. Galaxies are considered to be "starbursting" above the upper dashed line. Our sample of BCGs traces this Elbaz et al. (2011) MS, with scatter both above and below.

Muzzin et al. 2009, 2012; Wilson et al. 2009; Demarco et al. 2010). SpARCS employs the same technique as the Red Sequence Cluster Survey (Gladders & Yee 2005): it identifies regions of overdensities in red sequence (RS) galaxies by dual-filter imaging spanning the 4000 Å-break. To do this SpARCS obtained wide-field z' imaging over the Spitzer-SWIRE Legacy Survey fields which, in combination with Spitzer-IRAC Channel 1 (3.6 μm) imaging, brackets the break above $z \gtrsim 1$. This simultaneously provides a reliable redshift estimate ($\delta z = (z_{\rm spec} - z_{\rm RS})/(1 - z_{\rm spec}) = 0.075$, from ~600 spectroscopic redshifts) through a fit to the location of the red sequence in color space. Note that though designed to be sensitive to $z > 1$ clusters, the SpARCS catalog additionally contains many clusters at $z < 1$. Brightest cluster galaxies were identified at 3.6 μm, by taking the brightest galaxy within $z - 3.6\,\mu{\rm m} \pm 0.5$ of the red sequence of the cluster, and within 500 kpc of the centroid of the red sequence overdensity.

2.2. Target Selection

We select as ALMA targets BCGs that (a) lie in the southern/equatorial SWIRE fields ELAIS-S1 (ES1), CDFS, and XMM-LSS (XMM); (b) have a confirmed spectroscopic redshift from OzDES (the Australian Dark Energy Survey), taken using the AAOmega spectrograph and 2dF fiber positioner on the 4m Anglo-Australian Telescope (Lidman et al. 2020); (c) are IR-luminous (>100 μJy at 24 μm) and therefore star-forming (Figure 1); (d) come from SpARCS clusters with richness $N_{\rm gal} > 12$,[8] or roughly $M_{200} > 1 \times 10^{14} M_\odot$ (Wen et al. 2010, 2012; Capozzi et al. 2012; Andreon & Congdon 2014); and (e) have CO (2-1) lines that fall into an ALMA frequency band. These leave us with a sample of 33 BCGs.

[8] $N_{\rm gal}$ is defined as the background-subtracted number of galaxies (of any color) within 500 kpc of the cluster center brighter than ($M^*_{3.6\,\mu{\rm m}} + 1$).

2.3. Observations

Our observations were performed on the Atacama Large Millimeter Array (ALMA; Program ID 2019.1.01529.S, P.I. Webb) between 2019 November 22 and December 15. 30 BCGs were observed over a total of ~15 hr. Three BCGs were not observed because of the ALMA COVID-19 shutdown. We used ALMA bands 3, 4, and 5 (chosen to measure the CO (2-1) line) and configurations C43-1, C43-2, and C43-3. Data were calibrated using ALMA reduction pipeline scripts in CASA version 5.4.0. The nominal flux density calibration uncertainty for ALMA sources in these bands is ~5%–10% (Remijan et al. 2019). We cleaned the image cubes minimally with natural weighting and pixel sizes between 0.″2 and 0.″4, resulting in continuum-subtracted and primary beam-corrected images with 46″ to 90″ fields of view. We detected mostly unresolved CO emission at $\geqslant 3\sigma$ in 24 of 30 pointings, or at a detection rate of 80%. We chose the spectral resolution of each image cube individually, based on the strength of the detection. We show examples of three BCGs from our sample, spanning the observed redshift range and the observed S/N range, in Figure 2. A single BCG (CDFS-CO3) was additionally detected in radio continuum.

These observations were designed to be complete to a constant gas mass depth of $M_{\rm gas} \geqslant 10^{10} M_\odot$ at all redshifts. However, due to ALMA's minimum on-source integration time for a single science goal, many of the lower-redshift objects ($z \lesssim 0.6$) were observed for longer than necessary to achieve this molecular gas mass limit, resulting in 3σ image RMS depths between 1.2 mJy beam^{-1} ($z \sim 0.2$) and 0.6 mJy beam^{-1} ($z \sim 1.2$) over 100 km s^{-1} channels. The sensitivity to low gas masses thus increases at lower redshifts (see Figure 3).

2.4. CO (2-1) Molecular Gas Measurements

We determine galaxy gas masses in a three-step process. First, we generate first-pass spectral profiles by placing an elliptical aperture with semimajor and semiminor axes twice as large as those of the synthesized beam, and at the same orientation, at the center of each BCG. Spectra are fit with a single one-dimensional Gaussian profile. Second, we generate an integrated-intensity "Moment-0" map by collapsing the image cube over the velocity channels with significant emission as determined by this Gaussian fit to the spectral profile. We keep channels within 2σ (2 standard deviations) of the mean. We then fit potential signal in the Moment-0 map to a two-dimensional, elliptical Gaussian profile. Finally, we create a second one-dimensional spectral profile, extracted from an elliptical aperture with the parameters of the two-dimensional fitted profile; the new axis sizes are now three times the Gaussian full width at half maximum (FWHM).

We determine the mass of gas present in each galaxy by fitting the second-pass spectral profile to either single- or double-peaked Gaussians, depending on which gives the better fit according to its reduced χ^2 statistic. We take the area under this fit as the total line flux, and we convert this flux to a CO luminosity using Solomon & Vanden Bout (2005) Equation (3). We use galactic CO-to-H_2 conversion factors ($\alpha_{\rm CO} = 4.36\ M_\odot({\rm K\ km\ s^{-1}\ pc^2})^{-1}$, $r_{21} = 0.8$), as these are typical of galaxies on the star-forming main sequence (see Solomon et al. 1997; Freundlich et al. 2019) and allow easy comparison with existing H_2 masses in BCGs, such as those of Edge (2001) and Castignani et al. (2020). We note, however, that using different CO-to-H_2 conversion factors (for

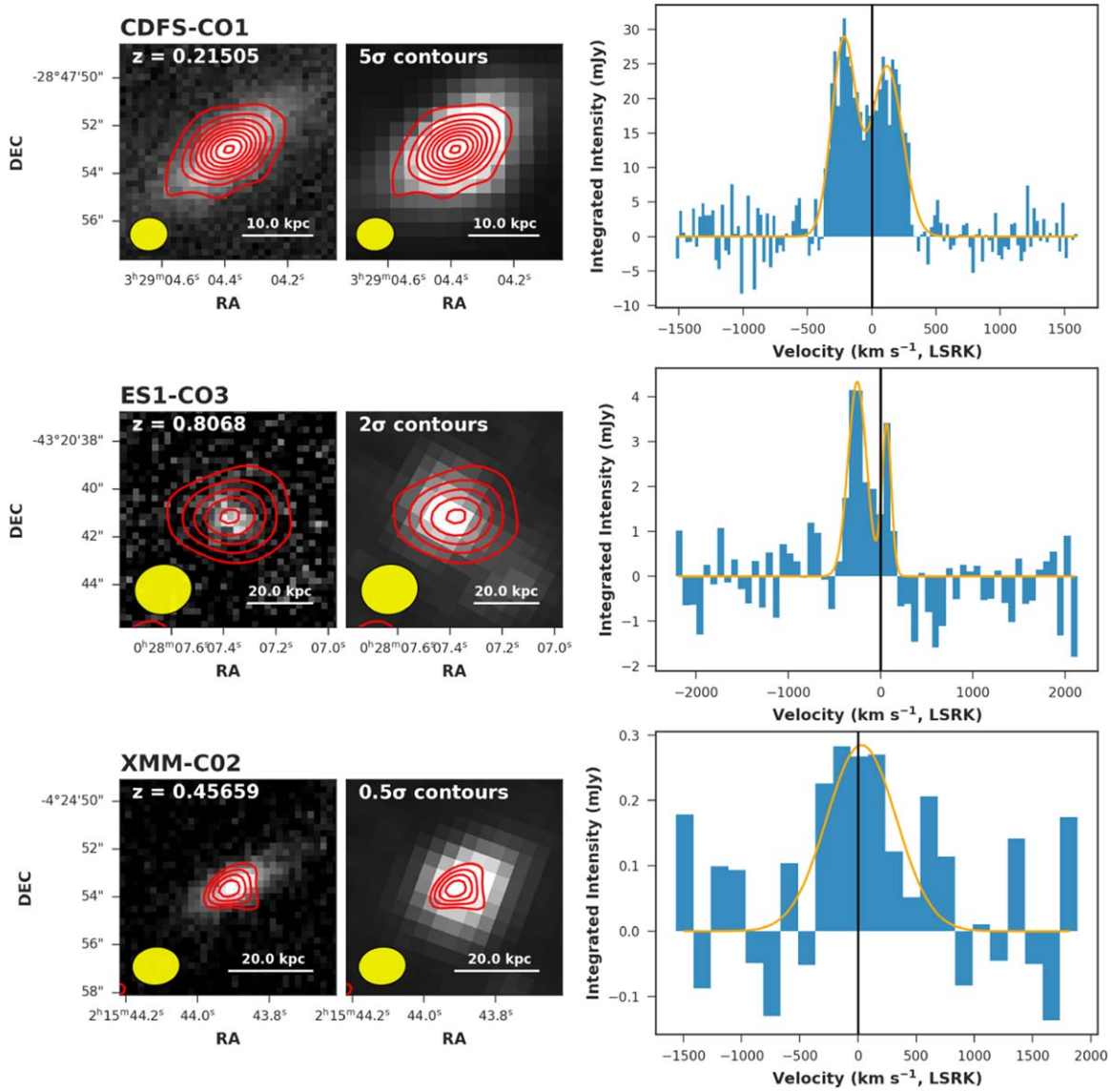

Figure 2. High-S/N (top), medium-S/N (center), and low-S/N (bottom) examples of our galaxies detected in CO, spanning the redshift range of our sample. Postage stamps are $9'' \times 9''$, showing the ALMA CO(2-1) integrated-intensity maps in S/N contours (red) overlaid on DES z-band imaging (left) and IRAC Channel 1 (3.6 μm) imaging (right). The ALMA synthesized beam is shown as the yellow ellipse. We show also the spectral profile for each galaxy, binned to the frequency used for calculations and centered around the OzDES spectroscopic redshift. One- or two-profile Gaussian fits are overlaid in orange.

example, $\alpha_{\rm CO} = 0.9$ and $r_{21} = 0.85$, typical of ultraluminous infrared galaxies; Bolatto et al. 2013) does not affect the results of this paper.

We treat the RMS noise in line-free channels ($\sim 7\sigma$ from the mean) of the spectral profile as the uncertainty in each flux value, and account for it while performing the least-squares Gaussian fits. We also search for CO emission in our six nondetections by stacking their spectra, centering each around the expected position of the CO line using the OzDES redshifts. The stack shows no significant emission, down to 3σ.

We determine gas mass limits on the six nondetections by collapsing the image cubes over a bandwidth equivalent to the average FWHM of the detected CO peaks ($356\,{\rm km\,s^{-1}}$) and taking the 3σ RMS value as an upper limit to the flux.

2.5. Stellar Masses and Star Formation Rates

We calculate the stellar mass of each galaxy using existing IRAC 3.6 μm photometry from SWIRE (Lonsdale et al. 2003) to determine the rest-frame K-band luminosity. We use an SED template from Bruzual & Charlot (2003) to calculate the K-correction, adopting an 11 Gyr simple stellar population with solar metallicity and a Salpeter initial mass function (IMF; Salpeter 1955). We note that adopting a template with a younger stellar population changes the average stellar mass values by at most 8%. This is within uncertainty and does not affect our results significantly, as they are primarily comparative. We determine a mass-to-light ratio of 0.83 by comparing our sample of 3.6 μm based values to more accurate values from a $griz/3.6\,\mu{\rm m}/4.5\,\mu{\rm m}$ (Abbott et al. 2018; Lonsdale et al. 2003) SED fit using FAST (Kriek et al. 2018). We take the scatter in this relation (0.3 dex) as the uncertainty in the stellar masses.

We also calculate star formation rates (SFRs) from SWIRE-MIPS 24 μm flux values (Lonsdale et al. 2003), using Kennicutt (1998) Equation 4 based on the luminosity at 24 μm ($L(24)$) from Chary & Elbaz (2001). We note that this

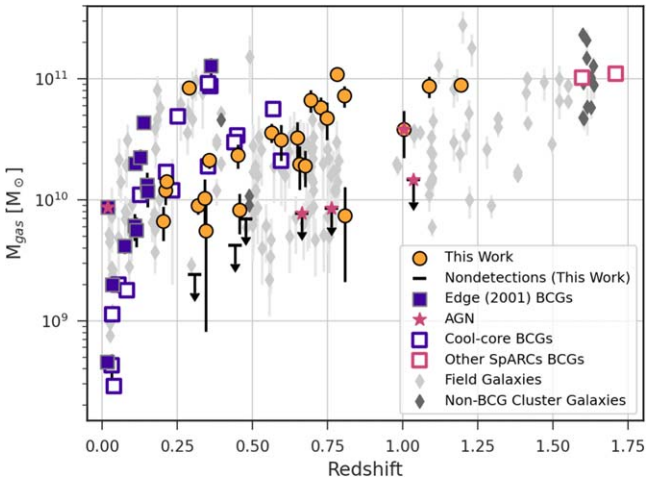

Figure 3. The current state of molecular gas measurements in galaxies across the literature. Our BCG sample (orange circles) is compared to other BCG CO measurements (squares) and non-BCG cluster (dark gray diamonds) and field (light gray diamonds) galaxies taken from the literature (Section 3.1). In the past, CO observations of BCGs have overwhelmingly targeted BCGs in cool-core clusters (empty purple squares). Pink stars indicate the BCGs in our analysis that fall into the Donley et al. (2012) AGN wedge. We pick out the Edge (2001) sample in particular (filled purple squares), as a large well-studied survey of low-redshift BCGs to compare to our data. The two pink squares are high-redshift BCGs in clusters whose dynamical state has not conclusively been determined—SpARCS1049 (Webb et al. 2017) and J0225-303 (Noble et al. 2019). Except for our own survey, we show only secure molecular gas detections, and not upper limits.

method is known to overestimate SFRs, particularly at high redshifts, but this generally occurs above the redshifts covered by our sample, at $z \sim 1.5$ (Elbaz et al. 2011). We achieve similar results with more modern SFR methods such as that of Rieke et al. (2009). We take the scatter of 0.15 dex described in Kennicutt (1998) to be the uncertainty in the SFRs. Because of SWIRE's 100 μJy MIPS limit, our sample is not complete in SFR—we can detect galaxies significantly ($\sim 1\sigma$) below the Elbaz et al. (2011) MS only to $z \sim 0.6$, and only starbursting galaxies above $z \sim 1$.

We present the properties of our BCG sample, including M_* and SFR values, in Table 1.

2.6. A Low-redshift BCG Comparison Sample

Edge (2001) introduces a sample of 34 BCGs at redshifts $\leqslant 0.45$ in clusters selected from ROSAT to have cooling flows. Of these, 16 galaxies are detected in CO, through a combination of CO(3-2) measurements made using the A3i reciever on JCMT, and CO(1-0) measurements made using the IRAM 30m telescope. Additionally, 12 BCGs have available 3.6 μm and 24 μm flux measurements. As the largest available sample of well-studied BCGs at low redshifts ($z_{\rm mean} = 0.12 \pm 0.09$), belonging to clusters with known dynamical states, this is a convenient sample with which to compare our BCG detections.

We take the molecular gas masses from Edge (2001), correcting the values for $H_0 = 70\,{\rm km\,s^{-1}\,Mpc^{-1}}$. Stellar masses and SFRs have been published for the Edge sample (O'Dea et al. 2008; Rawle et al. 2012); however, we choose to recalculate these values to allow for a homogeneous comparison between the Edge sample and our own. We therefore calculate both stellar masses and SFRs for these BCGs using the methods outlined in Section 2.5, including multiplying the SFR by the same FAST conversion factor, as the multiband photometry used in this SED fit is not available for the Edge galaxies. We take 3.6 μm flux values from Quillen et al. (2008), Yamagishi et al. (2010), and Landt et al. (2010), and MIPS 24 μm photometry from Shi et al. (2005), Quillen et al. (2008), Yamagishi et al. (2010), and the Spitzer Science Source List (Teplitz et al. 2010).

2.7. AGN Contamination

To check for AGN contamination, we compare the IRAC colors of both our sample (from SWIRE; Lonsdale et al. 2003) and the Edge sample (Quillen et al. 2008; Landt et al. 2010; Yamagishi et al. 2010) to the criteria described in Donley et al. (2012). We find that one CO-detected galaxy from each sample falls into the Donley AGN wedge, as well as the three nondetected galaxies at higher redshifts. These galaxies all show high sSFRs, and the 24 μm flux is likely dominated by the AGN; we thus exclude them from all further analysis but continue to show them on plots.

3. Results

The molecular gas properties of our BCG sample are presented in Table 1. With the largest and highest-z sample of significant molecular gas detections in BCGs assembled, we can investigate the reservoirs fueling their in situ star formation.

3.1. Gas Properties Compared to the Larger Galaxy Population

To place the gas in our BCGs in context, we compare in Figure 3 the molecular gas reservoirs found in our sample to those of a range of other galaxy types.[9] We pick out the Edge (2001) sample described in Section 2.6 as our main comparison sample. We indicate also the two other BCGs selected from SpARCS with confident molecular gas detections—SpARCS1049 (Webb et al. 2017), whose gas has recently been shown to be fed by a massive cooling flow (Hlavacek-Larrondo et al. 2020), and J0225-303 (Noble et al. 2019), which possibly represents a merging BCG based on rest-frame optical HST imaging, but whose cluster dynamical state has not been conclusively determined. The gap in coverage visible at $0.8 \lesssim z \lesssim 1.0$ corresponds to the redshift range within which CO lines fall into the gap in the ALMA frequency coverage between bands 3 and 4.

Figure 3 makes it immediately obvious that our sample reaches much higher redshift ranges than all previous BCG surveys. Few large-scale studies of molecular gas in BCGs have been undertaken, and those that do exist have been limited in distance by both CO instrument quality and the availability of cluster surveys at high redshifts. Above $z \sim 0.3$, most existing BCG gas masses come from targeted observations of known exceptional objects. These include the BCGs in A1664 ($z = 0.128$; Russell et al. 2014), A1835 ($z = 0.252$; McNamara et al. 2014), the Phoenix cluster ($z = 0.596$; Russell et al. 2017), and SpARCS 1049 ($z = 1.709$; Webb et al. 2017). Previous BCG studies include Edge (2001; described in detail in Section 2.6), who detected 16 BCGs, Salomé & Combes (2003), who detected 6

[9] Non-BCG cluster galaxies are taken from Noble et al. (2019, 2017) and Jablonka et al. (2013). Field galaxies are taken from Aravena et al. (2020), Bauermeister et al. (2013), Boogaard et al. (2020), Braun et al. (2011), Brownson et al. (2020), Combes et al. (2013), Decarli et al. (2016), Freundlich et al. (2019), Geach et al. (2011), and Hatsukade et al. (2020). Other BCG detections are from Castignani et al. (2020), Fogarty et al. (2019), McNamara et al. (2014), Russell et al. (2014), Russell et al. (2017), Salomé & Combes (2003), Tremblay et al. (2016), and Vantyghem et al. (2016).

Table 1
Properties of the ALMA-observed BCGs

SWIRE Patch (1)	R.A. (deg) (2)	Decl. (deg) (3)	$z_{\rm OzDES}$ (4)	$v_{\rm CO}$ Offset (km s^{-1}) (5)	$S_{\rm CO}\Delta v$ (Jy km s^{-1}) (6)	$M_{\rm gas}$ ($\times 10^{10}$, $M_\odot$) (7)	FWHM (km s^{-1}) (8)	SFR ($M_\odot$ yr^{-1}) (9)	M_* ($\times 10^{10}$, $M_\odot$) (10)
XMM-CO1	33.65927	−3.62736	1.0033	187 ± 100	0.50 ± 0.15	3.8 ± 1.6	147 ± 84	670^{+280}_{-200}	$22.9^{+14.0}_{-8.7}$
XMM-CO2	33.93287	−4.41511	0.4566	−150 ± 150	0.51 ± 0.20	0.8 ± 0.3	531 ± 127	27^{+11}_{-8}	$14.8^{+9.1}_{-5.6}$
XMM-CO3	34.64331	−5.01232	0.6410	162 ± 75	1.09 ± 0.26	3.3 ± 1.1	133 ± 63	34^{+14}_{-10}	$14.5^{+8.8}_{-5.5}$
XMM-CO4	34.79386	−3.72621	0.7634	⋯	<0.26	<0.9	⋯	410^{+169}_{-120}	$17.4^{+8.7}_{-5.8}$
XMM-CO5	34.87044	−4.11663	0.7826	−17 ± 25	2.36 ± 0.30	11.0 ± 1.3	271 ± 21	140^{+60}_{-40}	$13.4^{+8.2}_{-5.1}$
XMM-CO6	34.92392	−4.00916	0.2043	−27 ± 100	1.95 ± 0.57	0.7 ± 0.3	473 ± 84	$3.0^{+1.2}_{-0.9}$	$12.4^{+7.5}_{-4.7}$
XMM-CO7	35.22837	−3.54931	1.0346	⋯	<0.28	<1.7	⋯	420^{+168}_{-120}	$26.0^{+13.0}_{-8.6}$
XMM-CO8	36.11233	−5.60891	0.2120	−164 ± 50	3.88 ± 0.67	1.2 ± 0.3	503 ± 42	11^{+4}_{-3}	$6.5^{+4.0}_{-2.5}$
ES1-CO1	10.26937	−44.50626	0.3446	517 ± 200	0.65 ± 0.55	0.6 ± 0.5	188 ± 169	$6.1^{+2.5}_{-1.8}$	$22.2^{+13.5}_{-8.4}$
ES1-CO2	6.97816	−43.27981	1.0881	−103 ± 75	0.97 ± 0.20	8.7 ± 1.7	191 ± 63	75^{+31}_{-22}	$6.6^{+4.1}_{-2.5}$
ES1-CO3	7.03042	−43.3448	0.8068	−84 ± 25	1.48 ± 0.29	7.3 ± 1.4	403 ± 21	73^{+30}_{-21}	$9.8^{+6.0}_{-3.7}$
ES1-CO4	8.26314	−42.72425	0.7281	147 ± 100	1.37 ± 0.25	5.8 ± 1.3	541 ± 84	42^{+17}_{-12}	$6.5^{+4.0}_{-2.5}$
ES1-CO5	8.70355	−42.23410	0.4776	⋯	<0.41	<0.7	⋯	12^{+6}_{-4}	$15.6^{+7.8}_{-5.2}$
ES1-CO7	8.81504	−42.78926	0.6567	−314 ± 200	0.59 ± 0.21	2.0 ± 0.8	394 ± 169	28^{+11}_{-8}	$9.4^{+5.7}_{-3.6}$
ES1-CO8	8.81970	−42.68564	0.5640	−113 ± 50	1.58 ± 0.34	3.6 ± 0.6	253 ± 42	38^{+15}_{-11}	$5.5^{+3.4}_{-2.1}$
ES1-CO9	9.41918	−43.65286	1.1937	−83 ± 25	0.83 ± 0.11	8.9 ± 1.1	156 ± 21	250^{+100}_{-70}	$7.6^{+4.8}_{-2.9}$
ES1-CO10	9.76238	−44.36451	0.7474	-23 ± 100	1.13 ± 0.39	4.8 ± 1.6	494 ± 84	37^{+15}_{-10}	$15.2^{+9.3}_{-5.8}$
CDFS-CO1	52.26829	−28.79808	0.2891	−50 ± 25	14.33 ± 1.23	8.4 ± 0.7	558 ± 21	35^{+14}_{-10}	$15.8^{+9.6}_{-6.0}$
CDFS-CO2	52.90532	−28.40428	0.2151	170 ± 25	4.41 ± 0.27	1.42 ± 0.09	144 ± 21	35^{+14}_{-10}	$4.9^{+3.0}_{-1.8}$
CDFS-CO3	53.31982	−26.89622	0.8076	237 ± 200	0.18 ± 0.39	0.7 ± 0.5	564 ± 169	54^{+22}_{-15}	$12.9^{+7.9}_{-4.9}$
CDFS-CO4	53.46281	−27.33505	0.4511	−53 ± 75	1.59 ± 0.49	2.4 ± 0.5	493 ± 63	24^{+10}_{-7}	$20.6^{+12.6}_{-7.8}$
CDFS-CO5	53.48398	−27.25938	0.6948	−13 ± 100	1.87 ± 0.50	6.7 ± 1.4	432 ± 84	54^{+22}_{-15}	$11.5^{+7.1}_{-4.4}$
CDFS-CO6	53.55353	−28.41692	0.6643	⋯	<0.23	<0.8	⋯	180^{+69}_{-50}	$20.1^{+10.0}_{-6.7}$
CDFS-CO7	53.72804	−27.09096	0.6760	105 ± 200	0.55 ± 0.18	1.9 ± 0.6	448 ± 169	23^{+9}_{-6}	$11.6^{+7.1}_{-4.4}$
CDFS-CO8	53.77638	−29.26097	0.5950	185 ± 200	1.18 ± 0.39	3.1 ± 1.0	471 ± 169	73^{+30}_{-21}	$13.7^{+8.3}_{-5.2}$
CDFS-CO9	53.79709	−27.77951	0.4428	⋯	<0.15	<0.4	⋯	11^{+4}_{-3}	$16.0^{+8.0}_{-5.3}$
CDFS-CO10	53.83965	−29.61118	0.3079	⋯	<0.36	<0.3	⋯	$3.9^{+1.5}_{-1.1}$	$14.8^{+7.4}_{-4.9}$
CDFS-CO11	53.86995	−27.28562	0.3189	9 ± 25	1.23 ± 0.19	0.9 ± 0.1	56 ± 21	$9.5^{+3.9}_{-2.8}$	$5.6^{+3.4}_{-2.1}$
CDFS-CO12	53.89642	−27.26368	0.3422	73 ± 200	0.90 ± 0.46	1.0 ± 0.5	447 ± 169	$6.1^{+2.5}_{-1.8}$	$7.9^{+4.8}_{-3.0}$
CDFS-CO13	54.07105	−28.38037	0.3567	−93 ± 25	2.31 ± 0.34	2.1 ± 0.3	327 ± 21	36^{+15}_{-10}	$10.3^{+6.2}_{-3.9}$

Note. Spectroscopic redshifts (4) are taken from OzDES (see Section 2.3). The offset of the CO (2-1) velocity from this OzDES measurement is given in column (5). Measurements of the velocity-integrated CO (2-1) flux and the resulting gas masses are described in Section 2.4. The FWHM presented (8) are the single-Gaussian CO linewidths. SFR/M_* measurements are described in Section 2.5.

BCGs, with some overlap with the Edge (2001) sample, and Castignani et al. (2020), who detected five BCGs. Our sample of 24 BCGs is therefore large by comparison. Each of these studies had detection rates considerably lower than our own, likely because these studies either did not select their sample based on star formation (Edge 2001; Salomé & Combes 2003), or used a much weaker SFR criterion (Castignani et al. 2020).

3.2. Direct Comparison with Lower-redshift BCGs

In the field, tight correlations are known to exist between a galaxy's SFR, M_*, and gas mass (e.g., Genzel et al. 2010), suggesting a uniformity in baryon processing by field galaxies. To test if similar correlations exist in BCGs, we compare the sSFRs and molecular gas masses of our sample to those BCGs detected by Edge (2001) in Figure 4. Due to the sSFR depth limitations discussed in Section 2.5, we first analyze only the BCGs in our sample with redshifts below 0.6 (left panel). To determine if the two samples exhibit the same sSFR/$M_{\rm gas}$ properties, we fit a straight line to each sample separately in logarithmic space, using orthogonal distance regression (ODR) to account for uncertainties existing in both axes. We show fits, and their 1σ confidence regions, in Figure 4. With (logarithmic) slopes of 0.9 ± 0.3 and 0.9 ± 0.2 and offsets of -10 ± 3 and -10 ± 2, respectively, our sample of BCGs and the Edge (2001) sample display the same correlation below $z = 0.6$. As the slope in this plot is $\log({\rm SFR}/M_*)/\log(M_{\rm gas})$, a quantity related to the star formation efficiency (SFR/$M_{\rm gas}$), this suggests the two samples are processing molecular gas through similar means.

In the right panel of Figure 4, we plot the complete sample over all redshifts. Much of our sample to $z \sim 1.0$ falls into the 1σ confidence region of the fit to the Edge (2001) BCGs, suggesting that this similarity in gas processing could persist to higher redshifts, but this is inconclusive due to the small sample size and potential selection effects from limited sensitivity. The BCGs at redshifts above $z \sim 1.0$ seem to fall above this relation, suggesting a possible change in gas processing, but this is again somewhat speculative due to the limits of the sample. In both panels the CO nondetections are included for comparison. We note the three nondetections that fall off the plotted correlation all have sSFRs that are likely inflated by the presence of AGN.

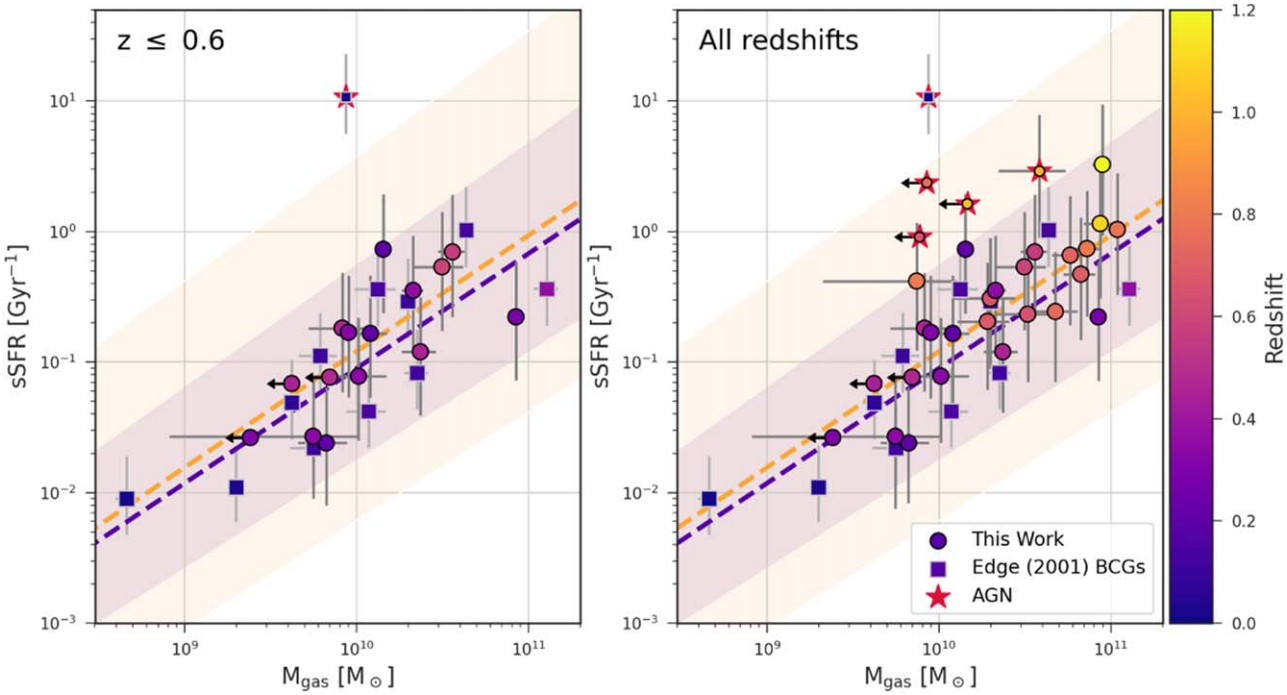

Figure 4. A comparison of the properties of BCGs found in this study (circles) to those reported in Edge (2001; squares). Points in both panels are colored according to their redshift. We show sSFR plotted against gas mass for both samples. The left panel contains only galaxies at $z \leqslant 0.6$ to prevent selection effects in either gas mass or SFR. ODR fits to the BCGs introduced in this work (orange) and to the Edge (2001) BCGs (purple) are shown with their 1σ confidence regions shaded. Fits to BCGs at $z \leqslant 0.6$ are also shown in the right panel, with the entire sample overlaid for reference. Galaxies not detected in CO (arrows) and those known to contain AGN (stars) are shown for reference, but are not included in the fits.

While we have worked to control for all potential systematic sSFR/$M_{\rm gas}$ differences between the two samples, there do remain several limitations. These include the different CO line transitions used in the $M_{\rm gas}$ values calculated by Edge (2001), the difficulty defining selection effects in this sample (which includes measurements from several different sources), and the incompleteness of our own sample. Additionally, while several large samples or field galaxies with molecular gas measurements do exist, such as ASPECS (Decarli et al. 2016), PHIBSS1 (Tacconi et al. 2013), and PHIBBS2 (Freundlich et al. 2019), few of these galaxies have both the 3.6 μm and 24 μm measurements necessary for rigorous comparison with the BCGs in this work, and those that do tend to fall above the MS. Ultimately, more CO data is required, for BCGs and field galaxies, particularly at high redshifts.

4. Discussion

We measure CO (2-1) in a sample of 30 star-forming BCGs, chosen from SpARCS. We find that 80% of our BCGs are detected in CO, suggesting that molecular gas is common in star-forming BCGs at high redshifts. While this is seemingly in contrast with the results of similar BCG surveys such as Castignani et al. (2020), we note that these previous studies imposed no SFR limit on their samples (see Section 3.1). We specifically target star-forming galaxies, and new stars cannot form without fuel.

Semi-analytic models suggest that strangulation, ram pressure stripping, and other cluster effects actively remove molecular gas from galaxies in dense environments (e.g., Gavazzi et al. 2006; De Lucia & Blaizot 2007), and therefore limit star formation. It is thus necessary to account for two different processes when analyzing BCG star formation—the process by which gas is deposited onto the BCG, and the mechanism by which the BCG converts that gas into stars. This distinction between gas feeding and processing in BCGs may have important implications, especially as similar theories have been proposed for the general galaxy population (see Behroozi et al. 2019).

In Figure 4, we show that our BCG sample at $z \leqslant 0.6$ has a remarkably similar correlation between $M_{\rm gas}$ and sSFR to that of Edge (2001), with nearly identical slopes. This implies that the two BCG samples are both processing their in situ molecular gas into stars with the same efficiency for a given stellar mass. This correlation exists at $z \leqslant 0.6$, and possibly to higher redshifts ($z \sim 1.0$), although this is uncertain due to the limiting depth of the sample, suggesting that many star-forming BCGs at $0 < z \leqslant 0.6$ may regulate the formation of these stars from gas in the same way, independent of their redshift or cluster properties. This is a picture of galaxy star formation that has been proposed for non-BCGs (e.g., Bouché et al. 2010; Dekel & Mandelker 2014).

Similarities in star formation processes between the Edge (2001) sample and our own have the potential to be very interesting, as the two samples differ in both selection method and cluster mass, in addition to the redshift difference discussed in Section 2.6. The Edge (2001) sample contains only BCGs from known cool-core clusters. In fact, all previous large BCG studies have selected galaxies either explicitly from known cool-core clusters (Edge 2001; Salomé & Combes 2003), or from X-ray surveys (Castignani et al. 2020). The parent, red-sequence selected SpARCS sample does not select clusters based on ICM state, and should therefore exhibit no cool-core selection effects. While the cool-core fraction varies depending on the selection criteria used, it should be $\lesssim$0.3 in the redshift range we study (McDonald et al. 2013).

We do note, however, that our BCG sample is selected on star formation, which may bias it toward cool-core clusters (e.g., Fogarty et al. 2015). If our galaxies are all cool-core cluster BCGs, and therefore fed by cooling flows, this is an interesting result on its own, as additional confirmation that the star formation we see in BCGs at $z \lesssim 0.6$ may be the result of those BCGs being fed molecular gas principally by cooling flows, instead of other possible scenarios such as gas-rich mergers. Unfortunately, we lack the X-ray measurements necessary to confirm the dynamical state of our clusters.

These speculations should not affect our main result—$M_{\rm gas}$ is a measurement of the amount of gas already in the galaxy. However, the CO-to-H_2 conversion factor used to determine molecular gas mass depends, among other things, on gas density (e.g., Bolatto et al. 2013). If some of our BCGs are dynamically unrelaxed post-mergers, this conversion factor could be affected, changing the relation. It is possible that we see this effect in Figure 4 at high redshifts, where BCGs tend to appear above the relation. This is in line with past work such as McDonald et al. (2016), which suggests that the mechanism fueling star formation changes from primarily cooling flows to gas-rich mergers in BCGs at $z \gtrsim 0.6$.

We cannot compare the cluster halo masses of our sample to those of Edge (2001) in depth, as we have no equivalent measurements to compare. We do, however, have cluster richnesses ($N_{\rm gal}$) measured from SpARCS (Webb et al. 2015) for our sample, and halo masses based on SDSS DR7 (Popesso et al. 2020; Yang et al. 2005) for the Edge (2001) BCGs. As $N_{\rm gal} = 12$ is roughly equal to $M_{200} \sim 1 \times 10^{14}$ (e.g., Andreon & Congdon 2014), our clusters have an average cluster mass $\sim (1.5 \pm 0.7) \times 10^{14}\, M_\odot$, compared to an average cluster mass of $\sim (1.3 \pm 0.9) \times 10^{15}\, M_\odot$ for the Edge (2001) sample. The clusters presented in Edge (2001) are therefore almost an order of magnitude more massive than ours.

It has been suggested that halo mass is directly related to central galaxy star formation, with the fraction of quenched central galaxies increasing with host halo mass (e.g., Behroozi et al. 2019). However, the star formation efficiency for galaxies at a given distance from the MS has been shown not to change with host halo mass (Popesso et al. 2020). We select only star-forming galaxies (i.e., galaxies at a fixed distance from the MS; Figure 1), so our values are unaffected by the fraction of quenched central galaxies at a given halo mass, and it is therefore unsurprising that the two BCG samples line up well despite their differing cluster masses.

5. Conclusions

We present the largest and highest-redshift study of molecular gas in BCGs to date. Using ALMA bands 3, 4, and 5, we study CO (2-1) in 30 SpARCS BCGs. We summarize our results as follows:

1. We find that molecular gas is common in star-forming BCGs at $0.2 \leqslant z \leqslant 1.2$, detecting gas reservoirs in 80% of our sample of 30 galaxies.
2. We note a clear $M_{\rm gas}$–sSFR trend is apparent in our sample. Below $z = 0.6$ this trend is consistent to 1σ with the sample of BCGs presented in Edge (2001). We therefore propose a scenario by which most BCGs below $z \sim 0.6$ process molecular gas into stars at a rate dependent on stellar mass, through mechanisms independent of redshift, and likely independent of cluster mass and cluster dynamical state. This scenario appears to persist to higher redshifts, but we require a larger and more complete sample to determine this conclusively.

The process by which these BCGs obtain molecular gas is still not clear. We require X-ray observations of our clusters to confirm both their dynamical state and their total mass. Still, as a large, high-z, collection of BCGs selected homogeneously and detected in CO, our sample offers an exciting means by which to study cluster evolution as a whole.

T.M.A.W. and D.A.D. acknowledge the support of the Natural Sciences and Engineering Research Council of Canada (NSERC) and the Fonds de Recherche Nature et Technologies Quebec (FRQNT).

This paper makes use of the following ALMA data: ADS/JAO.ALMA#2019.1.01529.S. ALMA is a partnership of ESO (representing its member states), NSF (USA) and NINS (Japan), together with NRC (Canada), MOST and ASIAA (Taiwan), and KASI (Republic of Korea), in cooperation with the Republic of Chile. The Joint ALMA Observatory is operated by ESO, AUI/NRAO, and NAOJ. This research has made use of the NASA/IPAC Infrared Science Archive, which is funded by the National Aeronautics and Space Administration and operated by the California Institute of Technology. Based in part on data acquired at the Anglo-Australian Telescope, under program A/2013B/012. We acknowledge the traditional owners of the land on which the AAT stands, the Gamilaraay people, and pay our respects to elders past and present. G.W. gratefully acknowledges support from the National Science Foundation through grant AST-1517863, from HST program number GO-15294, and from grant No. 80NSSC17K0019 issued through the NASA Astrophysics Data Analysis Program (ADAP). Support for program number GO-15294 was provided by NASA through a grant from the Space Telescope Science Institute, which is operated by the Association of Universities for Research in Astronomy, Incorporated, under NASA contract NAS5-26555.

This project used public archival data from the Dark Energy Survey (DES). Funding for the DES Projects has been provided by the U.S. Department of Energy, the U.S. National Science Foundation, the Ministry of Science and Education of Spain, the Science and Technology Facilities Council of the United Kingdom, the Higher Education Funding Council for England, the National Center for Supercomputing Applications at the University of Illinois at Urbana-Champaign, the Kavli Institute of Cosmological Physics at the University of Chicago, the Center for Cosmology and Astro-Particle Physics at the Ohio State University, the Mitchell Institute for Fundamental Physics and Astronomy at Texas A&M University, Financiadora de Estudos e Projetos, Fundação Carlos Chagas Filho de Amparo à Pesquisa do Estado do Rio de Janeiro, Conselho Nacional de Desenvolvimento Científico e Tecnológico and the Ministério da Ciência, Tecnologia e Inovação, the Deutsche Forschungsgemeinschaft, and the Collaborating Institutions in the Dark Energy Survey.

The Collaborating Institutions are Argonne National Laboratory, the University of California at Santa Cruz, the University of Cambridge, Centro de Investigaciones Energéticas, Medioambientales y Tecnológicas-Madrid, the University of Chicago, University College London, the DES-Brazil Consortium, the University of Edinburgh, the Eidgenössische Technische Hochschule (ETH) Zürich, Fermi National Accelerator Laboratory, the University of

Illinois at Urbana-Champaign, the Institut de Ciències de l'Espai (IEEC/CSIC), the Institut de Física d'Altes Energies, Lawrence Berkeley National Laboratory, the Ludwig-Maximilians Universität München and the associated Excellence Cluster Universe, the University of Michigan, the National Optical Astronomy Observatory, the University of Nottingham, The Ohio State University, the OzDES Membership Consortium, the University of Pennsylvania, the University of Portsmouth, SLAC National Accelerator Laboratory, Stanford University, the University of Sussex, and Texas A&M University.

Based in part on observations at Cerro Tololo Inter-American Observatory, National Optical Astronomy Observatory, which is operated by the Association of Universities for Research in Astronomy (AURA) under a cooperative agreement with the National Science Foundation.

ORCID iDs

Delaney A. Dunne https://orcid.org/0000-0002-5223-8315
Tracy M. A. Webb https://orcid.org/0000-0002-0104-9653
Allison Noble https://orcid.org/0000-0003-1832-4137
Christopher Lidman https://orcid.org/0000-0003-1731-0497
Adam Muzzin https://orcid.org/0000-0002-9330-9108
H. K. C. Yee https://orcid.org/0000-0003-4935-2720

References

Abazajian, K. N., Adelman-McCarthy, J. K., Agüeros, M. A., et al. 2009, ApJS, 182, 543
Abbott, T. M. C., Abdalla, F. B., Allam, S., et al. 2018, ApJS, 239, 18
Adelman-McCarthy, J. K., Agüeros, M. A., Allam, S. S., et al. 2008, ApJS, 175, 297
Andreon, S., & Congdon, P. 2014, A&A, 568, A23
Aravena, M., Boogaard, L., Gónzalez-López, J., et al. 2020, ApJ, 901, 79
Bauermeister, A., Blitz, L., Bolatto, A., et al. 2013, ApJ, 768, 132
Behroozi, P., Wechsler, R. H., Hearin, A. P., & Conroy, C. 2019, MNRAS, 488, 3143
Bolatto, A. D., Wolfire, M., & Leroy, A. K. 2013, ARA&A, 51, 207
Boogaard, L. A., Werf, P. V. D., Weiss, A., et al. 2020, ApJ, 902, 109
Bouché, N., Dekel, A., Genzel, R., et al. 2010, ApJ, 718, 1001
Braun, R., Popping, A., Brooks, K., & Combes, F. 2011, MNRAS, 416, 2600
Brownson, S., Belfiore, F., Maiolino, R., Lin, L., & Carniani, S. 2020, MNRAS: Letters, 498, L66
Bruzual, G., & Charlot, S. 2003, MNRAS, 344, 1000
Capozzi, D., Collins, C. A., Stott, J. P., & Hilton, M. 2012, MNRAS, 419, 2821
Castignani, G., Pandey-Pommier, M., Hamer, S. L., et al. 2020, A&A, 640, A65
Chary, R., & Elbaz, D. 2001, ApJ, 556, 562
Combes, F., Moiseev, A., & Reshetnikov, V. 2013, A&A, 554, A11
De Lucia, G., & Blaizot, J. 2007, MNRAS, 375, 2
Decarli, R., Walter, F., Aravena, M., et al. 2016, ApJ, 833, 70
Dekel, A., & Mandelker, N. 2014, MNRAS, 444, 2071
Demarco, R., Wilson, G., Muzzin, A., et al. 2010, ApJ, 711, 1185
Donley, J. L., Koekemoer, A. M., Brusa, M., et al. 2012, ApJ, 748, 142
Edge, A. 2001, MNRAS, 328, 762
Elbaz, D., Dickinson, M., Hwang, H. S., et al. 2011, A&A, 533, A119
Fabian, A., & Nulsen, P. 1977, MNRAS, 180, 479
Fogarty, K., Postman, M., Connor, T., Donahue, M., & Moustakas, J. 2015, ApJ, 813, 117
Fogarty, K., Postman, M., Li, Y., et al. 2019, ApJ, 879, 103
Freundlich, J., Combes, F., Tacconi, L. J., et al. 2019, A&A, 622, A105
Gavazzi, G., O'Neil, K., Boselli, A., & Van Driel, W. 2006, A&A, 449, 929
Geach, J. E., Smail, I., Moran, S. M., et al. 2011, ApJL, 730, L19
Genzel, R., Tacconi, L. J., Gracia-Carpio, J., et al. 2010, MNRAS, 407, 2091
Gladders, M. D., & Yee, H. K. 2005, ApJS, 157, 1
Gunn, J. E., Carr, M., Rockosi, C., et al. 1998, ApJ, 116, 3040
Hatsukade, B., Ohta, K., Hashimoto, T., et al. 2020, ApJ, 892, 42
Hernán-Caballero, A., Pérez-Fournon, I., Hatziminaoglou, E., et al. 2009, MNRAS, 395, 1695
Hlavacek-Larrondo, J., Rhea, C. L., Webb, T., et al. 2020, ApJL, 898, L50
Jablonka, P., Combes, F., Rines, K., Finn, R., & Welch, T. 2013, A&A, 557, A103
Kennicutt, Robert C., J. 1998, ARA&A, 36, 189
Kriek, M., van Dokkum, P. G., Labbé, I., et al. 2018, FAST: Fitting and Assessment of Synthetic Templates, version 1.0, Astrophysics Source Code Library, ascl:1803.008
Landt, H., Buchanan, C. L., & Barmby, P. 2010, MNRAS, 408, 1982
Lidman, C., Suherli, J., Muzzin, A., et al. 2012, MNRAS, 427, 550
Lidman, C., Tucker, B. E., Davis, T. M., et al. 2020, MNRAS, 496, 19
Lonsdale, C. J., Smith, H. E., Rowan-Robinson, M., et al. 2003, PASP, 115, 897
McDonald, M., Bayliss, M., Benson, B. A., et al. 2012, Natur, 488, 349
McDonald, M., Benson, B. A., Vikhlinin, A., et al. 2013, ApJ, 774, 23
McDonald, M., Stalder, B., Bayliss, M., et al. 2016, ApJ, 817, 86
McNamara, B. R., Russell, H. R., Nulsen, P. E. J., et al. 2014, ApJ, 785, 44
Menzel, M. L., Merloni, A., Georgakakis, A., et al. 2016, MNRAS, 457, 110
Muzzin, A., Wilson, G., Yee, H., et al. 2009, ApJ, 698, 1934
Muzzin, A., Wilson, G., Yee, H., et al. 2012, ApJ, 746, 188
Noble, A. G., McDonald, M., Muzzin, A., et al. 2017, ApJL, 842, L21
Noble, A. G., Muzzin, A., McDonald, M., et al. 2019, ApJ, 870, 56
O'Dea, C. P., Baum, S. A., Privon, G., et al. 2008, ApJ, 681, 1035
Popesso, P., Concas, A., Morselli, L., et al. 2020, MNRAS, 496, 2531
Quillen, A. C., Zufelt, N., Park, J., et al. 2008, ApJS, 176, 39
Rawle, T. D., Edge, A. C., Egami, E., et al. 2012, ApJ, 747, 29
Remijan, A., Biggs, A., Cortes, P., et al. 2019, ALMA Technical Handbook, ALMA Doc. 7.3, ver. 1.1, 7, https://almascience.nrao.edu/documents-and-tools/cycle7/alma-technical-handbook
Rieke, G. H., Alonso-Herrero, A., Weiner, B. J., et al. 2009, ApJ, 692, 556
Russell, H. R., McDonald, M., McNamara, B. R., et al. 2017, ApJ, 836, 130
Russell, H. R., McNamara, B. R., Edge, A. C., et al. 2014, ApJ, 784, 78
Salomé, P., & Combes, F. 2003, A&A, 412, 657
Salpeter, E. E. 1955, ApJ, 121, 161
Shi, Y., Rieke, G. H., Hines, D. C., et al. 2005, ApJ, 629, 88
Solomon, P., Downes, D., Radford, S., & Barrett, J. 1997, ApJ, 478, 144
Solomon, P., & Vanden Bout, P. 2005, ARA&A, 43, 677
Swinbank, A. M., Edge, A. C., Smail, I., et al. 2007, MNRAS, 379, 1343
Tacconi, L. J., Neri, R., Genzel, R., et al. 2013, ApJ, 768, 74
Teplitz, H. I., Capak, P., Brooke, T., et al. 2010, in ASP Conf. Ser. 434, Astronomical Data Analysis Software and Systems XIX, ed. Y. Mizumoto, K. I. Morita, & M. Ohishi (San Francisco, CA: ASP), 437
Tremblay, G. R., Oonk, J. B. R., Combes, F., et al. 2016, Natur, 534, 218
Vantyghem, A. N., McNamara, B. R., Russell, H. R., et al. 2016, ApJ, 832, 148
Webb, T. M. A., Lowenthal, J., Yun, M., et al. 2017, ApJL, 844, L17
Webb, T. M. A., Muzzin, A., Noble, A., et al. 2015, ApJ, 814, 96
Weedman, D. W., & Houck, J. R. 2009, ApJ, 698, 1682
Wen, Z., Han, J., & Liu, F. 2010, ApJS, 187, 272
Wen, Z., Han, J., & Liu, F. 2012, ApJS, 199, 34
Wilson, G., Muzzin, A., Yee, H., et al. 2009, ApJ, 698, 1943
Yamagishi, M., Kaneda, H., Ishihara, D., et al. 2010, PASJ, 62, 1085
Yang, X., Mo, H., Jing, Y., & Van Den Bosch, F. C. 2005, MNRAS, 358, 217